

# Spiral spin liquid in a frustrated honeycomb antiferromagnet: A single-crystal study of GdZnPO

Zongtang Wan,<sup>1,\*</sup> Yuqian Zhao,<sup>1,\*</sup> Xun Chen,<sup>1</sup> Zhaohua Ma,<sup>1</sup> Zikang Li,<sup>1</sup> Zhongwen Ouyang,<sup>1</sup> and Yuesheng Li<sup>1,†</sup>

<sup>1</sup>Wuhan National High Magnetic Field Center and School of Physics,  
Huazhong University of Science and Technology, 430074 Wuhan, China

The frustrated honeycomb spin model can stabilize a subextensively degenerate spiral spin liquid with nontrivial topological excitations and defects, but its material realization remains rare. Here, we report the experimental realization of this model in the structurally disorder-free compound GdZnPO. Using a single-crystal sample, we find that spin-7/2 rare-earth Gd<sup>3+</sup> ions form a honeycomb lattice with dominant second-nearest-neighbor antiferromagnetic and first-nearest-neighbor ferromagnetic couplings, along with easy-plane single-site anisotropy. This frustrated model stabilizes a unique spiral spin liquid with a degenerate contour around the K{1/3,1/3} point in reciprocal space, consistent with our experiments down to 30 mK, including the observation of a giant residual specific heat. Our results establish GdZnPO as an ideal platform for exploring the stability of spiral spin liquids and their novel properties, such as the emergence of low-energy topological defects on the sublattices.

*Introduction.*—In magnets, frustration can lead to the emergence of exotic phases such as spin liquids, which exhibit fractionalized excitations and topological order [1–3]. These phases intimately relate to significant scientific challenges, including understanding high-temperature superconductivity [4] and realizing topological quantum computation [5]. Frustrated magnetic interactions on lattices like triangular, kagome, and pyrochlore can result in extensively degenerate ground states with finite zero-point entropy per spin proportional to  $\ln(2S + 1)$  [6–8], where  $S$  is the spin quantum number. Such spin liquids can transition between different ground states by flipping only a few spins, reflecting a local nature of ground-state degeneracy [9]. In contrast, a spiral spin liquid (SSL) fluctuates cooperatively among subextensively degenerate spiral configurations, with ground-state wave vectors ( $\mathbf{Q}_G$ ) forming a continuous contour or surface in reciprocal space for two- (2D) or three-dimensional (3D) systems, respectively [10]. Transitioning between these configurations requires a global action on all spins [9]. Moreover, SSLs possess much lower ground-state degeneracy, with zero-point entropy per site proportional to  $\ln(2S + 1)/N^{1/d_0} \rightarrow 0$  in the thermodynamic limit, where  $N$  is the number of spins and  $d_0$  is the system’s dimension.

SSLs give rise to topological excitations/defects, such as spin vortices [11, 12] and momentum vortices [9, 13], which can be utilized in antiferromagnetic spintronics without leakage of magnetic fields [14–16], topologically protected quantum memory and logic operations [17], and the study of fracton gauge theory [18–20], among other applications. These defects also play a crucial role in determining the low-energy properties of the system [9]. SSLs on a frustrated honeycomb lattice may induce topological magnon bands and unconventional thermal Hall effects [21, 22]. Moreover, SSLs are proposed as a possible route to achieving the long-sought quantum spin liquids by tuning  $S$  from the classical ( $\rightarrow \infty$ ) to the quantum ( $= 1/2$ ) limit [23]. Despite extensive theoretical efforts, the explicit realization of SSLs in real materials remains rare, with only a few examples reported, such as the 3D diamond-lattice MnSc<sub>2</sub>S<sub>4</sub> [12, 16, 24, 25] and LiYbO<sub>2</sub> [26], the 3D buckled honeycomb Cs<sub>3</sub>Fe<sub>2</sub>Cl<sub>9</sub> [27, 28], the quasi-2D bilayer breathing-kagome Ca<sub>10</sub>Cr<sub>7</sub>O<sub>28</sub> [29, 30], and the

quasi-2D honeycomb FeCl<sub>3</sub> [31]. Moreover, most existing theoretical and experimental studies have focused on SSL systems with  $\mathbf{Q}_G$  around the  $\Gamma\{0,0\}$  point, leaving the (topological) properties of SSLs with  $\mathbf{Q}_G$  around non- $\Gamma$  points still unclear.

SSLs in the 2D  $J_1$ - $J_2$  frustrated honeycomb system can exist over a wide range of interaction parameters,  $1/2 > |J_2/J_1| > 1/6$  ( $\mathbf{Q}_G$  around the  $\Gamma$  point) and  $|J_2/J_1| > 1/2$  ( $\mathbf{Q}_G$  around the K{1/3,1/3} point) [21, 22, 32–35]. However, their experimental realization has only been explicitly reported in FeCl<sub>3</sub> to date [31]. In FeCl<sub>3</sub>, the honeycomb lattice is formed by transition-metal Fe<sup>3+</sup> ( $S = 5/2$ ) ions, with an interlayer separation of  $c/3 \sim 5.8$  Å, comparable to the second-nearest-neighbor intralayer distance  $a \sim 6.1$  Å. Due to the spatial delocalization of the 3d electrons, the interlayer couplings are non-negligible compared to  $J_2$ , complicating many-body modeling [31]. The spiral contour observed around the  $\Gamma$  point in FeCl<sub>3</sub> aligns with the ratio  $|J_2/J_1| \sim 0.36$  [31], but the honeycomb SSL with  $\mathbf{Q}_G$  around the K point has yet to be realized.

To approach the ideal  $J_1$ - $J_2$  honeycomb model, we investigate the rare-earth Gd<sup>3+</sup> ( $S = 7/2$ , orbital quantum number  $L = 0$ ) based honeycomb-lattice (or bilayer-triangular-lattice) antiferromagnet GdZnPO (Fig. 1), which has been successfully synthesized [36, 37] but remains understudied in terms of low-energy magnetism. Using a single-crystal sample, we determine the exchange Hamiltonian of GdZnPO, with first- and second-nearest-neighbor magnetic couplings  $J_1 \sim -0.39$  K and  $J_2 \sim 0.57$  K, respectively, and an easy-plane anisotropy  $D \sim 0.30$  K. Given  $|J_2/J_1| \sim 1.5$ , a SSL with  $\mathbf{Q}_G$  around the K point is expected to form, consistent with the observations of large magnetic specific heat and susceptibility in the low- $T$  limit. Monte Carlo (MC) simulations for GdZnPO reveal the emergence of well-defined spin vortices and antivortices, associated with local (sublattice) momentum vortices, on the sublattices. Future studies may explore Kitaev quantum spin liquids [38] and other quantum phases in structural siblings of GdZnPO with effective  $S = 1/2$  rare-earth ions instead.

*Methods.*—High-quality single crystals of GdZnPO were grown using a two-step method with NaCl/KCl flux. Magnetization and specific heat measurements were conducted be-

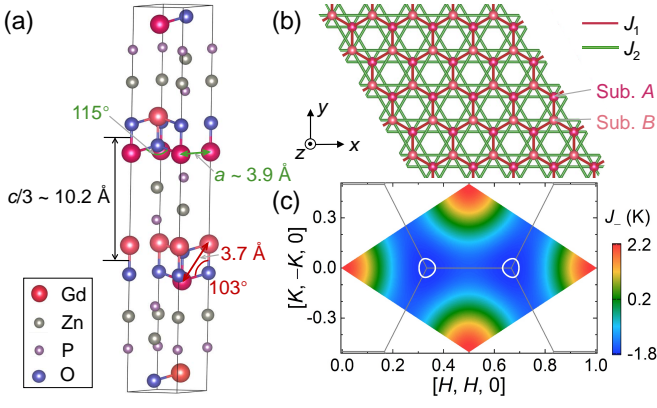


FIG. 1. (a) The GdZnPO crystal structure and (b) the honeycomb lattice in the  $ab$  plane formed by Gd<sup>3+</sup> ions. The inset in (b) defines the coordinate system for the spin components. (c) Wave-vector dependence of the lower eigenvalue of the interaction matrix,  $J_-$ , calculated from the GdZnPO spin Hamiltonian. The white lines indicate the spiral contour where  $J_-$  is minimized, and the grey lines mark Brillouin zone boundaries.

tween 1.8 and 300 K using magnetic and physical property measurement systems (Quantum Design). First-derivative electron spin resonance (ESR) spectra were obtained at 300 K and x-band frequencies ( $\sim 9.8$  GHz) using a continuous-wave spectrometer (Bruker EMXmicro-6/1). Pulsed-field ESR spectra were measured at 97 GHz down to  $\sim 2$  K at Wuhan National High Magnetic Field Center. Specific heat down to 53 mK and magnetization down to 30 mK were measured in a <sup>3</sup>He-<sup>4</sup>He dilution refrigerator. Standard MC simulations were conducted by slowly annealing from high to low temperatures on  $2 \times L_N^2$  clusters with periodic boundary conditions, where  $72 \geq L_N \geq 9$  [39].

*Exchange Hamiltonian.*—The crystal structure of GdZnPO, determined by x-ray diffraction (XRD) [39], is shown in Fig. 1(a). We propose GdZnPO as an ideal candidate for the frustrated honeycomb model for the following reasons: (1) Due to the highly localized nature of the  $4f$  electrons [40], it is sufficient to consider only the nearest-neighbor interactions,  $J_1$  (with  $|\text{Gd-Gd}| \sim 3.7$  Å) and  $J_2$  (with  $|\text{Gd-Gd}| \sim 3.9$  Å), while longer-range interactions with  $|\text{Gd-Gd}| \geq 5.4$  Å are negligible ( $\lesssim 0.016$  K). The nearest-neighbor exchanges  $J_1$  and  $J_2$  are mediated by O<sup>2-</sup> ions with the bond angles  $\angle\text{Gd-O-Gd} = 103^\circ$  and  $115^\circ$ , respectively, indicating  $J_2 > J_1$ . (2) The GdO honeycomb layers are spatially separated by a nonmagnetic ZnP bilayer, with an average distance of  $c/3 \sim 10.2$  Å, suggesting a strong 2D nature of the spin system. (3) Gd<sup>3+</sup> has the maximum  $S = 7/2$  among all existing SSL candidates, bringing the GdZnPO system closer to the classical prototype. (4) Gd<sup>3+</sup> is the only magnetic rare-earth ion with  $L = 0$ , making spin-spin interaction anisotropy due to spin-orbital coupling negligible. (5) The spatial isotropy of the honeycomb lattice is ensured by the  $R\bar{3}m$  space group symmetry of GdZnPO [Fig. 1(b)]. (6) No site-mixing struc-

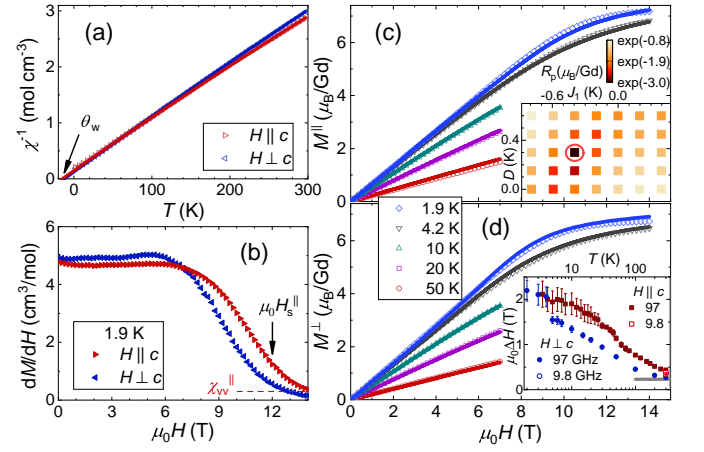


FIG. 2. Magnetic properties of GdZnPO. (a) Inverse magnetic susceptibilities measured at 1 T, with colored lines showing Curie-Weiss fits above  $\sim 20$  K. (b) Field dependence of susceptibility ( $dM/dH$ ) measured at 1.9 K. Combined MC fit to magnetization at various temperatures in fields parallel (c) and perpendicular (d) to the  $c$  axis. Inset of (c): Deviation  $R_p$  of experimental magnetization from theoretical values, with fixed  $\theta_w [\equiv -S(S+1)(J_1 + 2J_2)] = -12$  K. The red circle indicates the optimal parameters,  $J_1 \sim -0.4$  K and  $D \sim 0.3$  K. Inset of (d): Temperature dependence of ESR linewidths, with the gray line representing the calculated high-temperature limit.

tural disorder has been reported [36, 37], and our refinement of the single-crystal XRD data confirms this. Consequently, the notorious interaction randomness and resulting modeling complexity [41–43] are not applicable to GdZnPO. (7) The spatial localization of the  $4f$  electrons weakens  $J_1$  and  $J_2$ , allowing the GdZnPO spin system to be fully polarized by an achievable field ( $\leq 14$  T), enabling comprehensive magnetic investigations. (8) Single-crystal samples are available, enabling measurements of spin anisotropy.

The GdZnPO crystals are transparent insulators. The generic exchange Hamiltonian is given by

$$\mathcal{H} = J_1 \sum_{\langle j_0, j_1 \rangle} \mathbf{S}_{j_0} \cdot \mathbf{S}_{j_1} + J_2 \sum_{\langle\langle j_0, j_2 \rangle\rangle} \mathbf{S}_{j_0} \cdot \mathbf{S}_{j_2} + D \sum_{j_0} (S_{j_0}^z)^2 - \mu_0 H \parallel g \mu_B \sum_{j_0} S_{j_0}^z, \quad (1)$$

where  $D$  represents the single-site anisotropy for ions with  $S > 1/2$  [44]. At high temperatures ( $T \gtrsim 20$  K), the susceptibilities measured both parallel and perpendicular to the  $c$  axis are well fitted by the Curie-Weiss function [Fig. 2(a)],  $\chi = \mu_0 N_A \mu_B^2 g^2 S(S+1) / [3k_B(T - \theta_w)] + \chi_{\text{vV}}$ , where  $\chi_{\text{vV}}$  represents the nearly  $T$ -independent Van Vleck susceptibility [see Fig. 2(b)]. We obtained a Weiss temperature  $\theta_w = -12(1)$  K and  $g = 2.01(2)$ . The measured  $g$  factor is isotropic and close to the free electron value, confirming the absence of spin-orbital coupling due to  $L = 0$  in GdZnPO. A  $g \sim 2$  value is also detected in our ESR measurements [39].

At low temperatures and low fields, the longitudinal susceptibility  $\chi^{\parallel}$  is smaller than  $\chi^{\perp}$ . At higher fields, the spin

system is more easily polarized along the  $ab$  plane than along the  $c$  axis, as shown in Fig. 2(b). These observations indicate an easy-plane nature of the single-site anisotropy, with  $D > 0$ . From a combined fit to the magnetization data by minimizing  $R_p = \sqrt{\sum_j (M_j^{\text{exp}} - M_j^{\text{cal}})^2 / N_M}$  [Fig. 2(c) and 2(d)], we obtained  $J_1 \sim -0.39(2)$  K,  $J_2 \sim 0.57(2)$  K, and  $D \sim 0.30(2)$  K for GdZnPO, which forms the core findings of this work. Here,  $M_j^{\text{exp}}$  and  $M_j^{\text{cal}}$  represent the experimental and calculated magnetizations, respectively, and  $N_M$  is the number of data points. By fixing  $\theta_w \equiv -S(S+1)(J_1 + 2J_2)$  to the experimental value of  $-12$  K, we mapped  $R_p$ , which takes a minimum of  $0.05 \mu_B/\text{Gd}$  at the optimized values of  $J_1$  and  $D$  [see the inset of Fig. 2(c)]. Using the refined Hamiltonian, we calculated the ESR linewidth along the  $c$  axis in the high- $T$  limit,  $\mu_0 \Delta H (T \rightarrow \infty) = \sqrt{64\pi D^4 / (21J_1^2 + 42J_2^2 + 344D^2/63)} / (g\mu_B)$  [45, 46], which yielded  $\sim 0.23$  T, agreeing with the experimental values [see the inset of Fig. 2(d)].

*Spiral spin-liquid ansatz.*—We calculated the  $2 \times 2$  interaction matrix via the Fourier transform of Eq. (1) [47, 48]. Diagonalizing this matrix yield two eigenvalues, with the lower one,  $J_-(\mathbf{Q})$ , presented in Fig. 1(c).  $J_-$  reaches its minimum along the spiral contour at  $\mathbf{Q}_G = h_G \mathbf{b}_1 + k_G \mathbf{b}_2$ , where  $\cos(2\pi h_G) + \cos(2\pi k_G) + \cos(2\pi h_G + 2\pi k_G) = \frac{1}{2} (\frac{J_1^2}{4J_2^2} - 3)$  [39]. Here,  $\mathbf{b}_1$  and  $\mathbf{b}_2$  are the reciprocal vectors.

The spiral contour remains independent of the longitudinal field below the fully-polarized value,  $\mu_0 H_s^{\parallel} = S[2D + 3J_1 + 9J_2 + J_1^2/(4J_2)] / (g\mu_B)$  ( $\sim 12$  T), indicating the stability of the low- $T$  SSL phase against  $H^{\parallel}$  in GdZnPO. Moreover, the ratio  $J_2/|J_1| \sim 1.5$  approaches the  $J_2/|J_1| \rightarrow \infty$  limit, where  $J_2$  promotes a decoupled  $120^\circ$  coplanar order. Consequently, the spiral contour becomes nearly circular with a radius of  $|J_1|/(4\pi J_2)$  [49] around the K point, suggesting that the effective U(1) symmetry in reciprocal space may still stand. GdZnPO is thus a promising platform for exploring the fracton gauge theory [18–20], potentially after decomposing the honeycomb lattice into six sublattices (as discussed below).

*Low-energy spin excitations.*—The magnetic specific heat ( $C_m$ ) of GdZnPO was accurately determined by subtracting the specific heat of the nonmagnetic YZnPO as the lattice contribution [39]. Across all measured fields, the  $C_m$  data show no significant Schottky upturns down to the lowest temperatures [Fig. 3(a)], and the Gd nuclear contribution is negligible [50]. At 0 T,  $C_m$  exhibits a peak around  $T^* \sim 2$  K, attributed to the formation of coplanar spin configurations [Fig. 4(b)] and a crossover between the high- $T$  paramagnetic phase and the SSL, accompanied by the spontaneous breaking of chiral symmetry [Fig. 4(c)] [35, 39]. Below  $\sim T^*$ ,  $C_m$  remains large and nearly independent of the longitudinal field at  $\mu_0 H^{\parallel} \lesssim 8$  T. Below  $\sim 0.5$  K,  $C_m$  follows the behavior  $C_m \sim C_0 + C_1 T$ , with  $C_0 = 1.20(4)$   $\text{JK}^{-1}/\text{mol}$  and  $C_1 = 2.74 \pm 0.16$   $\text{JK}^{-2}/\text{mol}$ , for  $\mu_0 H^{\parallel} \lesssim 8$  T. In sharp contrast, at a longitudinal field of 11.8 T (close to  $\mu_0 H_s^{\parallel}$ ),  $C_m$  drops significantly and approaches zero as  $T \rightarrow 0$  K. From the low-

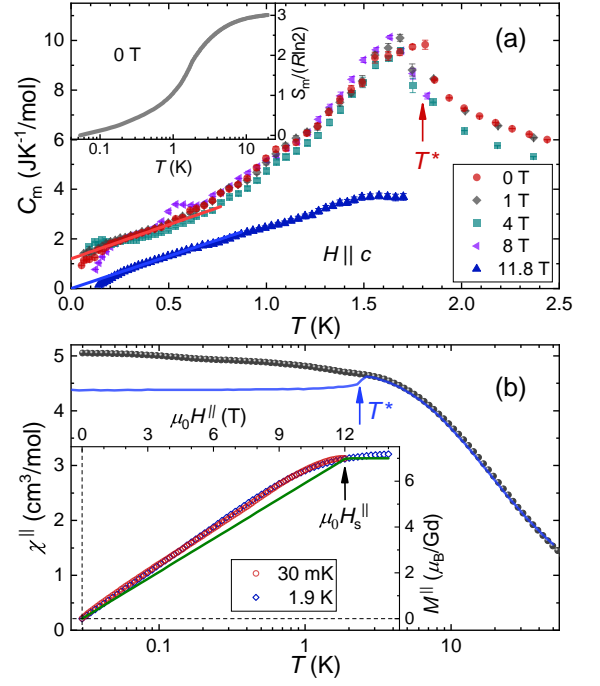


FIG. 3. Low-temperature properties of GdZnPO. (a) Temperature dependence of magnetic specific heat under various fields along the  $c$  axis. The red and blue lines are guides to the eye; the inset shows magnetic entropy at 0 T. (b) Temperature dependence of magnetic susceptibility ( $M^{\parallel}/H^{\parallel}$ ) measured with  $\mu_0 H^{\parallel} = 1$  T along the  $c$  axis. The line represents the MC simulation. Inset of (b): Longitudinal magnetization measured at 30 mK and 1.9 K, with the green line showing the 0 K calculation using the classical SSL ansatz.

est measured temperature  $T_{\min} = 53$  mK ( $\ll |J_1|S^2$ ) up to  $\sim 20$  K ( $\gg |J_1|S^2$ ), the system releases an entropy [ $S_m(T) = \int_{T_{\min}}^T C_m(T')/T' dT'$ ]  $\sim 3R \ln 2 = R \ln(2S+1)$  [see the inset of Fig. 3(a)], indicating the absence of zero-point entropy in GdZnPO. Additionally, the small  $S_m$  suggests that the system approaches its ground states at  $T \lesssim 0.15$  K.

Similarly, the magnetic susceptibility becomes constant at  $\chi_0^{\parallel} \sim 5$   $\text{cm}^3/\text{mol}$  as  $T \rightarrow 0$  K [Fig. 3(b)]. At low temperatures, the magnetization exhibits full polarization at  $H^{\parallel} \sim H_s^{\parallel}$  and nearly linear polarization at  $\mu_0 H^{\parallel} \lesssim 9$  T [inset of Fig. 3(b)].

*Discussion.*—The measured residual specific heat  $C_0 = 1.20(4)$   $\text{JK}^{-1}/\text{mol}$  at  $\mu_0 H^{\parallel} \lesssim 8$  T in GdZnPO is unusually large, a phenomenon not previously reported in strongly correlated magnets to our knowledge. For instance, the 3D SSL candidates  $\text{MnSc}_2\text{S}_4$  and  $\text{LiYbO}_2$  exhibit magnetic specific heat  $C_m \sim 0.2$  and  $0.01$   $\text{JK}^{-1}/\text{mol}$ , respectively (after removing nuclear contributions), at temperatures as low as  $\sim 0.1$  K [51, 52]. The 2D SSL candidates  $\text{Ca}_{10}\text{Cr}_7\text{O}_{28}$  and  $\text{FeCl}_3$  show  $C_m \sim 0.16$  and  $0.02$   $\text{JK}^{-1}/\text{mol}$  at  $\sim 0.037$  and  $0.6$  K, respectively [53, 54]. Rare-earth spin-ice  $\text{Dy}_2\text{Ti}_2\text{O}_7$ , which exhibits significant zero-point entropy, has  $C_m \sim 0.044$   $\text{JK}^{-1}/\text{mol}$  at  $\sim 0.4$  K [8]. The rare-earth gapless spin-liquid candidate  $\text{YbMgGaO}_4$  shows  $C_m \sim 0.2$   $\text{JK}^{-1}/\text{mol}$  at 60



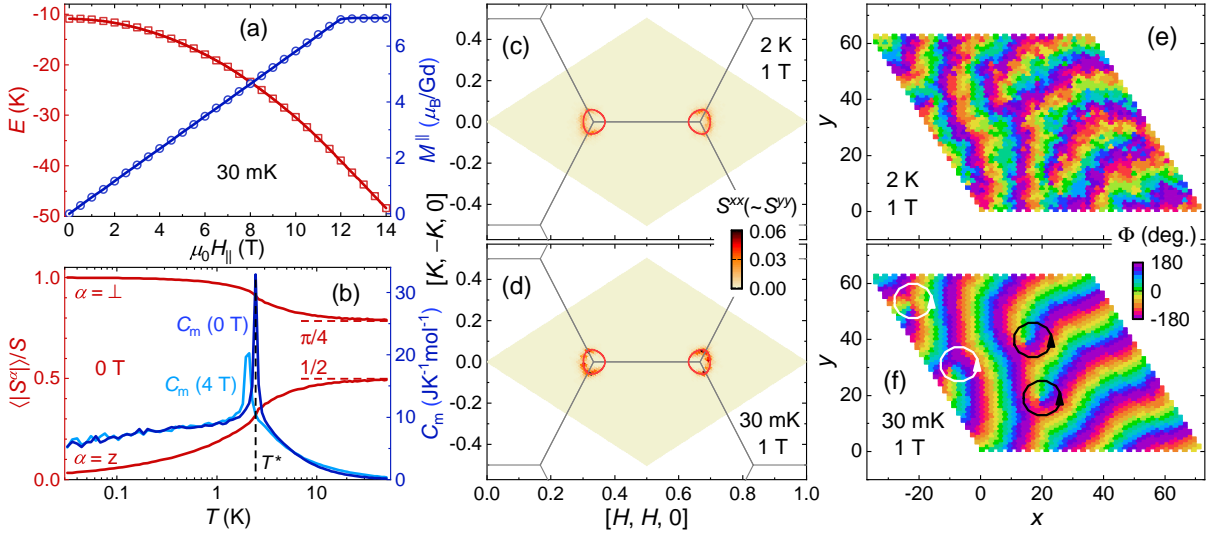


FIG. 4. MC simulations for GdZnPO. (a) Energy per spin (red) and magnetization (blue). Scatters represent MC results at 30 mK, while colored lines are analytical results at 0 K using the SSL ansatz. (b) Temperature dependence of average absolute spin components at 0 T (solid red curves:  $\langle |S^{\perp}| \rangle \equiv \langle \sqrt{(S^x)^2 + (S^y)^2} \rangle$  and  $\langle |S^z| \rangle$ ) and specific heat [dark blue:  $C_m(0 \text{ T})$ ; light blue:  $C_m(\mu_0 H^{\parallel} = 4 \text{ T})$ ] calculated via MC simulations. Dashed red lines indicate high-temperature limits of  $\langle |S^{\perp}| \rangle = \pi S/4$  and  $\langle |S^z| \rangle = S/2$  [39]. Spin structure factors at 2 K (c) and 30 mK (d) in  $\mu_0 H^{\parallel} = 1 \text{ T}$ . Red lines show the spiral contour; grey lines mark Brillouin zone boundaries. Spin configurations projected onto the  $ab$  plane,  $\Phi = -i \ln \frac{S^x + iS^y}{\sqrt{(S^x)^2 + (S^y)^2}}$ , calculated at 2 K (e) and 30 mK (f) in  $\mu_0 H^{\parallel} = 1 \text{ T}$  on sublattice A I [39]. White and black circles mark spin vortices [ $C_s = \oint d\Phi(\mathbf{r})/(2\pi) = 1$ ] and antivortices ( $C_s = -1$ ), with arrows indicating the integral direction.

mK [55]. These  $C_m$  values are considerably smaller than the  $C_0$  observed in GdZnPO. A slightly faster drop in  $C_m$  is visible below  $\sim 0.15 \text{ K}$  at 0 T [Fig. 3(a)], possibly indicating a precursor to “order by disorder” [32]. However, zero-field  $C_m \sim 1 \text{ JK}^{-1}/\text{mol}$  remains large even at 53 mK, and applying a field of  $\mu_0 H^{\parallel} = 1$  or 4 T can prevent the drop down to  $\sim 65 \text{ mK}$ . The rapid decrease in  $C_m$  observed at 8 and 11.8 T below  $\sim 0.2 \text{ K}$  can be attributed to a gap opening due to the Zeeman interaction, as the spin system approaches full polarization.

Due to the presence of the spiral contour, the specific heat behavior of  $C_m \sim C_0 + C_1 T$  had been predicted for a generic SSL within the spherical approximation [10, 24]. Moreover, our classical MC simulations also indicate that  $C_m \rightarrow \text{constant}$  as  $T \rightarrow 0 \text{ K}$  [see Fig. 4(b)]. Therefore, the observation of a giant  $C_0$  in GdZnPO is distinctive among all existing strongly correlated magnets and should serve as a strong signature of the spiral contour and SSL. Furthermore, the sudden drop of  $C_m$  from  $\sim 8$  to 11.8 T, suggesting that GdZnPO could be utilized in demagnetization cooling to mK temperatures [56, 57], especially when a moderate-to-strong magnetic field is unavoidable.

The SSL ansatz is confirmed by unbiased MC calculations for both energy and magnetization, as shown in Fig. 4(a). The low- $T$  limit of specific heat calculated by the classical model,  $C_0^{\text{cal}} \sim 5 \text{ JK}^{-1}/\text{mol}$  [Fig. 4(b)], is significantly larger than the measured  $C_0 \sim 1.2 \text{ JK}^{-1}/\text{mol}$ . Additionally, the low- $T$  limit of susceptibility calculated using the classical SSL ansatz,  $\chi_0^{\parallel, \text{cal}} = \mu_0 N_A g^2 \mu_B^2 / [2D + 3J_1 + 9J_2 + J_1^2 / (4J_2)] + \chi_{\text{VV}}^{\parallel}$  [58]

$\sim 4.4 \text{ cm}^3/\text{mol}$ , is smaller than the measured  $\chi_0^{\parallel} \sim 5 \text{ cm}^3/\text{mol}$ . These discrepancies at low temperatures may be attributed to the quantization of spin and quantum fluctuations in the real material GdZnPO, despite  $S = 7/2$  being relatively large. Additionally, weak perturbations beyond Eq. (1) in the real material could also contribute to these discrepancies.

Next, we examine the stability of the SSL in GdZnPO as the temperature decreases. Neither the specific heat nor the susceptibility shows clear evidence of further magnetic order below  $T^*$  (Fig. 3). As the temperature decreases from  $\sim T^*$  to 30 mK, the spin structure factor calculated at the classical level does not exhibit further concentration at special points [compare Figs. 4(d) with 4(c)], which contrasts sharply with conventional magnetic orders. Our simulations for GdZnPO, consistent with previously reported results [35], suggest that “order by disorder” is still prevented by thermal fluctuations down to 30 mK ( $\sim 0.006 |J_1| S^2$ ), aligning with experimental observations. The occurrence of “order by disorder” at lower temperatures remains a possibility and warrants further investigation.

Finally, we examine the low-energy topological defects. The SSL phase in GdZnPO approximates a nearly decoupled three-sublattice  $120^\circ$  coplanar order in the  $ab$  plane. Consequently, we decompose the honeycomb lattice into six triangular sublattices:  $A \text{ I}$ ,  $A \text{ II}$ ,  $A \text{ III}$ ,  $B \text{ I}$ ,  $B \text{ II}$ , and  $B \text{ III}$ . At low temperatures, spin vortices and antivortices become evident, with spin winding numbers  $C_s = 1$  and  $-1$ , respectively, as illustrated in Fig. 4(f). These topological defects persist at

$T \sim T^*$ , as shown in Fig. 4(e). The orientations of neighboring spins on different sublattices are locked together, causing the positions of vortices and antivortices to remain fixed across different sublattices. Additionally, the corresponding local (sublattice) momentum vortices [9] are observed around the positions of spin vortices and antivortices on the sublattices, as shown in Fig. S6 of [39]. Since these sublattices are discernible in the SSL phase below  $\sim T^*$ , their topological configurations may be utilized in developing small-scale antiferromagnetic spintronic devices [14–16].

**Conclusions.**—We establish GdZnPO as an ideal candidate for the frustrated honeycomb model, which stabilizes a distinctive SSL with a spiral contour around the K point. Experimental observations, including the giant residual specific heat  $C_0 \sim 1.2 \text{ JK}^{-1}/\text{mol}$ , provide strong evidence for the formation of SSL down to extremely low temperatures. The distinctive SSL supports the emergence of low-energy spin vortices and antivortices, as well as momentum vortices, on the sublattices at low temperatures. This may be a significant step towards realizing antiferromagnetic spintronic devices.

**Acknowledgments.**—We gratefully acknowledge Shang Gao, Zhengxin Liu, Haijun Liao, and Changle Liu for helpful discussion. This work was supported by the National Key R&D Program of China (Grant No. 2023YFA1406500), the National Natural Science Foundation of China (Nos. 12274153 and U20A2073), and the Fundamental Research Funds for the Central Universities (No. HUST: 2020kfyXJJS054).

---

\* These authors contributed equally to this work

† [yuesheng.li@hust.edu.cn](mailto:yuesheng.li@hust.edu.cn)

- [1] L. Balents, “Spin liquids in frustrated magnets,” *Nature* **464**, 199 (2010).
- [2] L. Savary and L. Balents, “Quantum spin liquids: a review,” *Rep. Prog. Phys.* **80**, 016502 (2016).
- [3] Y. Zhou, K. Kanoda, and T.-K. Ng, “Quantum spin liquid states,” *Rev. Mod. Phys.* **89**, 025003 (2017).
- [4] P. W. Anderson, “The resonating valence bond state in  $\text{La}_2\text{CuO}_4$  and superconductivity,” *Science* **235**, 1196 (1987).
- [5] C. Nayak, S. H. Simon, A. Stern, M. Freedman, and S. Das Sarma, “Non-Abelian anyons and topological quantum computation,” *Rev. Mod. Phys.* **80**, 1083 (2008).
- [6] G. H. Wannier, “Antiferromagnetism. the triangular Ising net,” *Phys. Rev.* **79**, 357 (1950).
- [7] K. Kanô and S. Naya, “Antiferromagnetism. the kagomé Ising net,” *Prog. Theor. Phys.* **10**, 158 (1953).
- [8] A. P. Ramirez, A. Hayashi, R. J. Cava, R. Siddharthan, and B. S. Shastry, “Zero-point entropy in ‘spin ice’,” *Nature* **399**, 333 (1999).
- [9] H. Yan and J. Reuther, “Low-energy structure of spiral spin liquids,” *Phys. Rev. Res.* **4**, 023175 (2022).
- [10] X.-P. Yao, J. Q. Liu, C.-J. Huang, X. Wang, and G. Chen, “Generic spiral spin liquids,” *Front. Phys.* **16**, 53303 (2021).
- [11] L. Seabra, P. Sindzingre, T. Momoi, and N. Shannon, “Novel phases in a square-lattice frustrated ferromagnet:  $\frac{1}{3}$ -magnetization plateau, helicoidal spin liquid, and vortex crystal,” *Phys. Rev. B* **93**, 085132 (2016).
- [12] S. Gao, O. Zaharko, V. Tsurkan, Y. Su, J. S. White, G. S. Tucker, B. Roessli, F. Bourdarot, R. Sibille, D. Chernyshov, T. Fennell, A. Loidl, and C. Rüegg, “Spiral spin-liquid and the emergence of a vortex-like state in  $\text{MnSc}_2\text{S}_4$ ,” *Nat. Phys.* **13**, 157 (2017).
- [13] M. G. Gonzalez, A. Fancelli, H. Yan, and J. Reuther, “Magnetic properties of the spiral spin liquid and surrounding phases in the square lattice XY model,” *Phys. Rev. B* **110**, 085106 (2024).
- [14] T. Jungwirth, X. Marti, P. Wadley, and J. Wunderlich, “Antiferromagnetic spintronics,” *Nat. Nanotechnol.* **11**, 231 (2016).
- [15] V. Baltz, A. Manchon, M. Tsoi, T. Moriyama, T. Ono, and Y. Tserkovnyak, “Antiferromagnetic spintronics,” *Rev. Mod. Phys.* **90**, 015005 (2018).
- [16] S. Gao, H. D. Rosales, F. A. G. Albarracín, V. Tsurkan, G. Kaur, T. Fennell, P. Steffens, M. Boehm, P. Čermák, A. Schneidewind, E. Ressouche, D. C. Cabra, C. Rüegg, and O. Zaharko, “Fractional antiferromagnetic skyrmion lattice induced by anisotropic couplings,” *Nature* **586**, 37 (2020).
- [17] N. Y. Yao, C. R. Laumann, A. V. Gorshkov, H. Weimer, L. Jiang, J. I. Cirac, P. Zoller, and M. D. Lukin, “Topologically protected quantum state transfer in a chiral spin liquid,” *Nat. Commun.* **4**, 1585 (2013).
- [18] M. Pretko, “Subdimensional particle structure of higher rank  $U(1)$  spin liquids,” *Phys. Rev. B* **95**, 115139 (2017).
- [19] R. M. Nandkishore and M. Hermele, “Fractons,” *Annu. Rev. Condens. Matter Phys.* **10**, 295 (2019).
- [20] M. Pretko, X. Chen, and Y. You, “Fracton phases of matter,” *Int. J. Mod. Phys. A* **35**, 2030003 (2020).
- [21] S. A. Owerre, “Topological magnon bands and unconventional thermal Hall effect on the frustrated honeycomb and bilayer triangular lattice,” *J. Phys.: Condens. Matter* **29**, 385801 (2017).
- [22] K. Fujiwara, S. Kitamura, and T. Morimoto, “Thermal Hall responses in frustrated honeycomb spin systems,” *Phys. Rev. B* **106**, 035113 (2022).
- [23] N. Niggemann, M. Hering, and J. Reuther, “Classical spiral spin liquids as a possible route to quantum spin liquids,” *J. Phys.: Condens. Matter* **32**, 024001 (2019).
- [24] D. Bergman, J. Alicea, E. Gull, S. Trebst, and L. Balents, “Order-by-disorder and spiral spin-liquid in frustrated diamond-lattice antiferromagnets,” *Nat. Phys.* **3**, 487 (2007).
- [25] Y. Iqbal, T. Müller, H. O. Jeschke, R. Thomale, and J. Reuther, “Stability of the spiral spin liquid in  $\text{MnSc}_2\text{S}_4$ ,” *Phys. Rev. B* **98**, 064427 (2018).
- [26] J. N. Graham, N. Qureshi, C. Ritter, P. Manuel, A. R. Wildes, and L. Clark, “Experimental evidence for the spiral spin liquid in  $\text{LiYbO}_2$ ,” *Phys. Rev. Lett.* **130**, 166703 (2023).
- [27] S. Gao, C. Pasco, O. Omar, Q. Zhang, D. M. Pajerowski, F. Ye, M. Frontzek, A. F. May, M. B. Stone, and A. D. Christianson, “Codimension-two spiral spin-liquid in the effective honeycomb-lattice compound  $\text{Cs}_3\text{Fe}_2\text{Cl}_9$ ,” (2024), [arXiv:2405.18973](https://arxiv.org/abs/2405.18973).
- [28] Y. Ishii, Y. Narumi, Y. Matsushita, M. Oda, T. Kida, M. Hagiwara, and H. K. Yoshida, “Field-induced successive phase transitions in the  $J_1 - J_2$  buckled honeycomb antiferromagnet  $\text{Cs}_3\text{Fe}_2\text{Cl}_9$ ,” *Phys. Rev. B* **103**, 104433 (2021).
- [29] R. Pohle, H. Yan, and N. Shannon, “Theory of  $\text{Ca}_{10}\text{Cr}_7\text{O}_{28}$  as a bilayer breathing-kagome magnet: Classical thermodynamics and semiclassical dynamics,” *Phys. Rev. B* **104**, 024426 (2021).
- [30] H. Takahashi, C.-C. Hsu, F. Jerzembeck, J. Murphy, J. Ward, J. D. Enright, J. Knapp, P. Puphal, M. Isobe, Y. Matsumoto, H. Takagi, J. C. S. Davis, and S. J. Blundell, “Spiral spin liquid noise,” (2024), [arXiv:2405.02075](https://arxiv.org/abs/2405.02075).
- [31] S. Gao, M. A. McGuire, Y. Liu, D. L. Abernathy, C. Cruz,

- M. Frontzek, M. B. Stone, and A. D. Christianson, "Spiral spin liquid on a honeycomb lattice," *Phys. Rev. Lett.* **128**, 227201 (2022).
- [32] A. Mulder, R. Ganesh, L. Capriotti, and A. Paramekanti, "Spiral order by disorder and lattice nematic order in a frustrated Heisenberg antiferromagnet on the honeycomb lattice," *Phys. Rev. B* **81**, 214419 (2010).
- [33] S. Okumura, H. Kawamura, T. Okubo, and Y. Motome, "Novel spin-liquid states in the frustrated Heisenberg antiferromagnet on the honeycomb lattice," *J. Phys. Soc. Jpn.* **79**, 114705 (2010).
- [34] T. Shimokawa, T. Okubo, and H. Kawamura, "Multiple- $q$  states of the  $J_1$ - $J_2$  classical honeycomb-lattice Heisenberg antiferromagnet under a magnetic field," *Phys. Rev. B* **100**, 224404 (2019).
- [35] C.-J. Huang, J. Q. Liu, and G. Chen, "Spiral spin liquid behavior and persistent reciprocal kagome structure in frustrated van der Waals magnets and beyond," *Phys. Rev. Res.* **4**, 013121 (2022).
- [36] A. T. Nientiedt and W. Jeitschko, "Equiatomic quaternary rare earth element zinc pnictide oxides RZnPO and RZnAsO," *Inorg. Chem.* **37**, 386 (1998).
- [37] H. Lincke, R. Glaum, V. Ditrach, M. Tegel, D. Johrendt, W. Hermes, M. H. Möller, T. Nilges, and R. Pöttgen, "Magnetic, optical, and electronic properties of the phosphide oxides REZnPO (RE = Y, La-Nd, Sm, Gd, Dy, Ho)," *Z. Anorg. Allg. Chem.* **634**, 1339 (2008).
- [38] A. Kitaev, "Anyons in an exactly solved model and beyond," *Ann. Phys.* **321**, 2 (2006).
- [39] See *Supplementary Material for detailed information about experimental and numerical procedures, which includes Refs. [59–66]*.
- [40] Y. Li, G. Chen, W. Tong, L. Pi, J. Liu, Z. Yang, X. Wang, and Q. Zhang, "Rare-earth triangular lattice spin liquid: A single-crystal study of YbMgGaO<sub>4</sub>," *Phys. Rev. Lett.* **115**, 167203 (2015).
- [41] Y. Li, D. Adroja, R. I. Bewley, D. Voneshen, A. A. Tsirlin, P. Gegenwart, and Q. Zhang, "Crystalline electric-field randomness in the triangular lattice spin-liquid YbMgGaO<sub>4</sub>," *Phys. Rev. Lett.* **118**, 107202 (2017).
- [42] Y. Li, S. Bachus, H. Deng, W. Schmidt, H. Thoma, V. Hutanu, Y. Tokiwa, A. A. Tsirlin, and P. Gegenwart, "Partial up-down order with the continuously distributed order parameter in the triangular antiferromagnet TmMgGaO<sub>4</sub>," *Phys. Rev. X* **10**, 011007 (2020).
- [43] J. Liu, L. Yuan, X. Li, B. Li, K. Zhao, H. Liao, and Y. Li, "Gapless spin liquid behavior in a kagome Heisenberg antiferromagnet with randomly distributed hexagons of alternate bonds," *Phys. Rev. B* **105**, 024418 (2022).
- [44] J. Liu, B. Liu, L. Yuan, B. Li, L. Xie, X. Chen, H. Zhang, D. Xu, W. Tong, J. Wang, and Y. Li, "Frustrated magnetism of the triangular-lattice antiferromagnets  $\alpha$ -CrOOH and  $\alpha$ -CrOOD," *New J. Phys.* **23**, 033040 (2021).
- [45] T. G. Castner and M. S. Seehra, "Antisymmetric exchange and exchange-narrowed electron-paramagnetic-resonance linewidths," *Phys. Rev. B* **4**, 38 (1971).
- [46] A. Zorko, S. Nellutla, J. van Tol, L. C. Brunel, F. Bert, F. Duc, J.-C. Trombe, M. A. de Vries, A. Harrison, and P. Mendels, "Dzyaloshinsky-Moriya anisotropy in the spin-1/2 kagome compound ZnCu<sub>3</sub>(OH)<sub>6</sub>Cl<sub>2</sub>," *Phys. Rev. Lett.* **101**, 026405 (2008).
- [47] J. N. Reimers, A. J. Berlinsky, and A.-C. Shi, "Mean-field approach to magnetic ordering in highly frustrated pyrochlores," *Phys. Rev. B* **43**, 865–878 (1991).
- [48] J. A. M. Paddison and M. J. Cliffe, "Discovering classical spin liquids by topological search of high symmetry nets," (2024), [arXiv:2406.06416](https://arxiv.org/abs/2406.06416).
- [49] Here, the lengths of the reciprocal vectors were set as unit, with  $|\mathbf{b}_1| = |\mathbf{b}_2| = 1$ .
- [50] The nuclear specific heat of Gd follows  $C_N = AT^{-2}$ , where  $A$  slightly varies among compounds. For example,  $A = 1.37 \times 10^{-4}$  and  $1.75 \times 10^{-4}$  JK/mol-Gd have been reported for Gd<sub>2</sub>Sn<sub>2</sub>O<sub>7</sub> [67] and Gd<sub>2</sub>(Ti<sub>1-x</sub>Zr<sub>x</sub>)<sub>2</sub>O<sub>7</sub> ( $x = 0.02$  and  $0.15$ ) [68], respectively. At  $T \geq 53$  mK,  $C_N \lesssim 0.05$  JK<sup>-1</sup>/mol, much smaller than the measured  $C_m \gtrsim 1$  JK<sup>-1</sup>/mol in GdZnPO, confirming the negligible nuclear contribution.
- [51] V. Fritsch, J. Hemberger, N. Büttgen, E.-W. Scheidt, H.-A. Krug von Nidda, A. Loidl, and V. Tsurkan, "Spin and orbital frustration in MnSc<sub>2</sub>S<sub>4</sub> and FeSc<sub>2</sub>S<sub>4</sub>," *Phys. Rev. Lett.* **92**, 116401 (2004).
- [52] M. M. Bordelon, C. Liu, L. Posthuma, E. Kenney, M. J. Graf, N. P. Butch, A. Banerjee, S. Calder, L. Balents, and S. D. Wilson, "Frustrated Heisenberg  $J_1$ - $J_2$  model within the stretched diamond lattice of LiYbO<sub>2</sub>," *Phys. Rev. B* **103**, 014420 (2021).
- [53] J. Sonnenschein, C. Balz, U. Tutsch, M. Lang, H. Ryll, J. A. Rodriguez-Rivera, A. T. M. Nazmul Islam, B. Lake, and J. Reuther, "Signatures for spinons in the quantum spin liquid candidate Ca<sub>10</sub>Cr<sub>7</sub>O<sub>28</sub>," *Phys. Rev. B* **100**, 174428 (2019).
- [54] M. Z. Tahir and G. O. Zimmerman, "Zero-field cooled specific heat of FeCl<sub>3</sub> intercalated graphite," *AIP Conf. Proc.* **850**, 1245 (2006).
- [55] Y. Li, H. Liao, Z. Zhang, S. Li, F. Jin, L. Ling, L. Zhang, Y. Zou, L. Pi, Z. Yang, J. Wang, Z. Wu, and Q. Zhang, "Gapless quantum spin liquid ground state in the two-dimensional spin-1/2 triangular antiferromagnet YbMgGaO<sub>4</sub>," *Sci. Rep.* **5**, 16419 (2015).
- [56] Y. Tokiwa, S. Bachus, K. Kavita, A. Jesche, A. A. Tsirlin, and P. Gegenwart, "Frustrated magnet for adiabatic demagnetization cooling to milli-Kelvin temperatures," *Commun. Mater.* **2**, 42 (2021).
- [57] J. Xiang, C. Zhang, Y. Gao, W. Schmidt, K. Schmalzl, C.-W. Wang, B. Li, N. Xi, X.-Y. Liu, H. Jin, G. Li, J. Shen, Z. Chen, Y. Qi, Y. Wan, W. Jin, W. Li, P. Sun, and G. Su, "Giant magnetocaloric effect in spin supersolid candidate Na<sub>2</sub>BaCo(PO<sub>4</sub>)<sub>2</sub>," *Nature* **625**, 270 (2024).
- [58]  $\chi_{\text{v}}^{\parallel} \sim 0.3$  cm<sup>3</sup>/mol at low temperatures.
- [59] B. Li, X. Chen, Y. Zhao, Z. Ma, Z. Wan, and Y. Li, "Proximate Tomonaga-Luttinger liquid in a spin-1/2 ferromagnetic XXZ chain compound," *Phys. Rev. Mater.* **8**, 074410 (2024).
- [60] B. Li, Z. Wan, Y. Song, Z. Ma, Y. Zhao, J. Wang, and Y. Li, "Frustrated magnetism of the spin-1 kagome antiferromagnet  $\beta$ -BaNi<sub>3</sub>(VO<sub>4</sub>)<sub>2</sub>(OH)<sub>2</sub>," *J. Phys.: Condens. Matter* **35**, 505801 (2023).
- [61] X. Y. Yue, Z. W. Ouyang, J. F. Wang, Z. X. Wang, Z. C. Xia, and Z. Z. He, "Magnetization and ESR studies on Cu<sub>4</sub>(OH)<sub>6</sub>FCl: An antiferromagnet with a kagome lattice," *Phys. Rev. B* **97**, 054417 (2018).
- [62] X. P. Jin, Z. W. Ouyang, X. C. Liu, T. T. Xiao, J. J. Cao, Z. X. Wang, Z. C. Xia, and W. Tong, "Two-sublattice description of the dimer-trimer chain compound Li<sub>2</sub>Cu<sub>5</sub>Si<sub>4</sub>O<sub>14</sub>: High-field magnetization and ESR studies," *Phys. Rev. B* **104**, 174423 (2021).
- [63] Z. Zhang, Y. Cai, J. Kang, Z. Ouyang, Z. Zhang, A. Zhang, J. Ji, F. Jin, and Q. Zhang, "Anisotropic exchange coupling and ground state phase diagram of Kitaev compound YbOCl," *Phys. Rev. Res.* **4**, 033006 (2022).
- [64] Y. Shimizu, Y. Kono, T. Sugiyama, S. Kittaka, Y. Shimura,

- A. Miyake, D. Aoki, and T. Sakakibara, "Development of high-resolution capacitive Faraday magnetometers for sub-Kelvin region," *Rev. Sci. Instrum.* **92**, 123908 (2021).
- [65] Y. Zhao, Z. Ma, Z. He, H. Liao, Y.-C. Wang, J. Wang, and Y. Li, "Quantum annealing of a frustrated magnet," *Nat. Commun.* **15**, 3495 (2024).
- [66] Y. Li, S. Bachus, B. Liu, I. Radelytskyi, A. Bertin, A. Schneidewind, Y. Tokiwa, A. A. Tsirlin, and P. Gegenwart, "Rearrangement of uncorrelated valence bonds evidenced by low-energy spin excitations in  $\text{YbMgGaO}_4$ ," *Phys. Rev. Lett.* **122**, 137201 (2019).
- [67] J. A. Quilliam, K. A. Ross, A. G. Del Maestro, M. J. P. Gingras, L. R. Corruccini, and J. B. Kycia, "Evidence for gapped spin-wave excitations in the frustrated  $\text{Gd}_2\text{Sn}_2\text{O}_7$  pyrochlore antiferromagnet from low-temperature specific heat measurements," *Phys. Rev. Lett.* **99**, 097201 (2007).
- [68] D. Q. Liao, M. R. Lees, D. W. Baker, D. M. Paul, and G. Balakrishnan, "Magnetic order in geometrically frustrated  $\text{Gd}_2(\text{Ti}_{1-x}\text{Zr}_x)_2\text{O}_7$  ( $x = 0.02$  and  $0.15$ ) single crystals," *Phys. Rev. B* **83**, 064403 (2011).

## Supplementary material

### Spiral spin liquid in a frustrated honeycomb antiferromagnet: A single-crystal study of GdZnPO

Zongtang Wan,<sup>1,\*</sup> Yuqian Zhao,<sup>1,\*</sup> Xun Chen,<sup>1</sup> Zhaohua Ma,<sup>1</sup> Zikang Li,<sup>1</sup> Zhongwen Ouyang,<sup>1</sup> and Yuesheng Li<sup>1,†</sup>

<sup>1</sup>*Wuhan National High Magnetic Field Center and School of Physics,  
Huazhong University of Science and Technology, 430074 Wuhan, China*

We present here:

#### I. Sample synthesis and characterization.

Fig. S1. Typical crystal and x-ray diffraction patterns.

Fig. S2. Specific heat measurements.

Fig. S3. Electron spin resonance spectra.

Tab. S1. Single-crystal structure refinement.

#### II. Spiral spin-liquid ansatz.

#### III. Monte Carlo simulations and low-energy topological defects.

Fig. S4. Calculated spin structure factors at various temperatures.

Fig. S5. Calculated spin configuration projected onto the  $ab$  plane for all six sublattices.

Fig. S6. Local momentum vortices on all six sublattices.

Fig. S7. Calculated spin configuration on the  $A$  and  $B$  sublattices and on the entire honeycomb lattice, and entropy increase.

---

\* These authors contributed equally to this work

† [yuesheng\\_li@hust.edu.cn](mailto:yuesheng_li@hust.edu.cn)



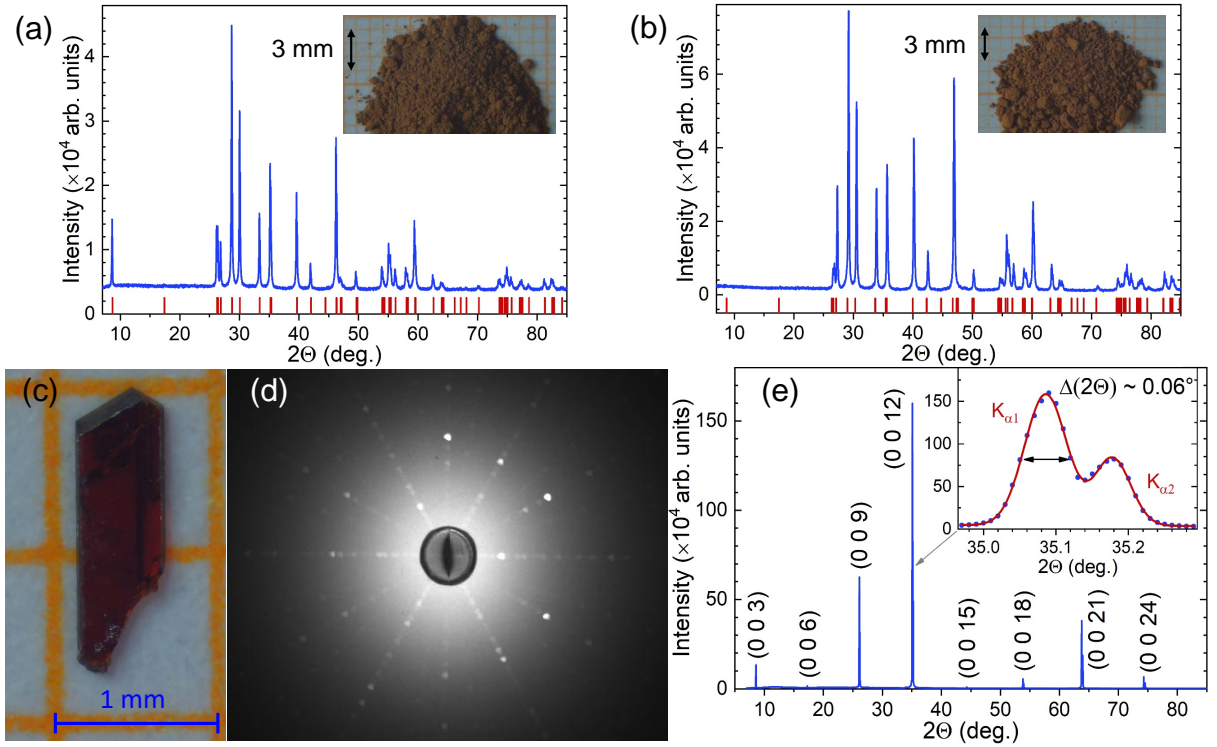


FIG. S1. Powder XRD patterns of precursor GdZnPO (a) and YZnPO (b), with red bars indicating calculated reflection positions. Insets show the respective powders. (c) Typical as-grown single crystal of GdZnPO. (d) Laue XRD pattern on the  $ab$  plane. (e) XRD pattern on the  $ab$  plane. Inset: Zoomed view of the (0 0 12) reflection with a two-Gaussian fit; the fitted full width at half maximum is listed.

## I. SAMPLE SYNTHESIS AND CHARACTERIZATION

We grew high-quality single crystals of GdZnPO in two steps. First, polycrystalline GdZnPO precursor was synthesized via a solid-phase method using stoichiometric mixtures of gadolinium (99.9%, Aladdin), zinc oxide (99.99%, Aladdin), and red phosphorus (99.999%, Alfa Aesar). The materials were mixed, pressed into pellets in an argon-filled glove box, and sealed in vacuum ( $\leq 1.0 \times 10^{-5}$  bar) in quartz tubes. The tubes were heated to  $950^\circ\text{C}$  for three days, yielding brown GdZnPO powders [see Fig. S1(a)], confirmed by powder x-ray diffraction (XRD, Cu  $K_\alpha$ ,  $\bar{\lambda} = 1.5418 \text{ \AA}$ , Rigaku) for phase purity and air insensitivity. Second, single crystals were grown using the flux method. The GdZnPO powders were mixed with equimolar NaCl/KCl flux in a 1:50:50 mole ratio, sealed in quartz tubes under vacuum, and heated to  $1050^\circ\text{C}$  for ten days. The excess flux was removed with highly pure water, and GdZnPO showed water insensitivity at room temperatures.

The as-grown GdZnPO single crystals are reddish-brown and transparent [see Fig. S1(c)]. Laue photographs of the crystals show sharp reflections [LAUESYS\_V\_674, Photonic Science & Engineering Ltd, see Fig. S1(d)], and the XRD Bragg reflections can be fitted with Gaussian-peak functions, with a full width at half maximum of  $\sim 0.06^\circ$ , only slightly larger than the instrumental resolution of  $0.05^\circ$  [see Fig. S1(e)]. These results indicate the high quality of the single-crystal samples. No additional reflections were observed in the XRD patterns, confirming the pure phase of GdZnPO. The structural reflection positions [Fig. S1(e)] yield a lattice parameter  $c = 30.58(2) \text{ \AA}$ , consistent with the previously reported value [1]. Furthermore, the GdZnPO crystal structure determined by single-crystal XRD (Mo  $K_\alpha$ ,  $\bar{\lambda} = 0.71073 \text{ \AA}$ , XtaLAB mini II, Rigaku) and refinements (Table S1) agrees well with the reference [1].

The powder of the nonmagnetic reference compound YZnPO was synthesized using a similar solid-phase method. Yttrium (99.99%, Aladdin), zinc oxide (99.99%, Aladdin), zinc (99.99%, Aladdin), and red phosphorus (99.999%, Alfa Aesar) were mixed in a molar ratio of 1:0.85:0.19:1.035, following the same procedure as for the GdZnPO powder synthesis. The phase purity of YZnPO was confirmed by powder XRD [see Fig. S1(b)]. The specific heat of YZnPO, shown in Fig. S2(a), represents the lattice contribution and was subtracted from the total specific heat of GdZnPO in the main text.

The specific heat above 1.8 K was measured using a physical property measurement system (PPMS, Quantum Design). The setup for milli-Kelvin specific heat measurements is shown in Fig. S2(b) [2–4]. Temperatures ranging from 53 mK to 1.8 K were achieved using a  $^3\text{He}$ - $^4\text{He}$  dilution refrigerator (KELMX-400, Oxford Instruments). Ac resistance Bridges & temperature controllers (model 372, Lakeshore) were used to measure thermometer resistances, control the heat sink temperature, and apply

TABLE S1. Structure refinement of the single-crystal XRD data measured at 300 K. Occupancy fractions were set to “1” for all atoms, following the methodology in Ref. [1].

crystal size used in refinement	0.11×0.11×0.05 mm
space group	$R\bar{3}m$
$a$ ( $\equiv b$ )	3.9180(4) Å
$c$	30.531(3) Å
cell volume, $Z = 6$	405.9±0.1 Å <sup>3</sup>
Gd: $z$ ( $x \equiv y \equiv 0$ )	0.38035(8)
$U_{11}(\equiv U_{22}), U_{33}, U_{12}$ ( $U_{13} \equiv U_{23} \equiv 0$ )	0.0120(9), 0.006(1), 0.0060(4)
Zn: $z$ ( $x \equiv 0$ and $y \equiv 0$ )	0.8038(2)
$U_{11}(\equiv U_{22}), U_{33}, U_{12}$ ( $U_{13} \equiv U_{23} \equiv 0$ )	0.019(2), 0.017(3), 0.009(1)
P: $z$ ( $x \equiv 0$ and $y \equiv 0$ )	0.1113(5)
$U_{11}(\equiv U_{22}), U_{33}, U_{12}$ ( $U_{13} \equiv U_{23} \equiv 0$ )	0.018(4), 0.009(6), 0.009(2)
O: $z$ ( $x \equiv 0$ and $y \equiv 0$ )	0.304(1)
$U_{11}(\equiv U_{22}), U_{33}, U_{12}$ ( $U_{13} \equiv U_{23} \equiv 0$ )	0.01(1), 0.04(2), 0.006(5)
$h$ range	-5 → 5
$k$ range	-4 → 5
$l$ range	-42 → 18
number of reflections ( $I > 0$ )	523
number of reflections ( $I > 3\sigma_I$ )	485
$R(F)$ ( $I > 3\sigma_I$ )	7.2%
$R_w(F)$ ( $I > 3\sigma_I$ )	9.6%

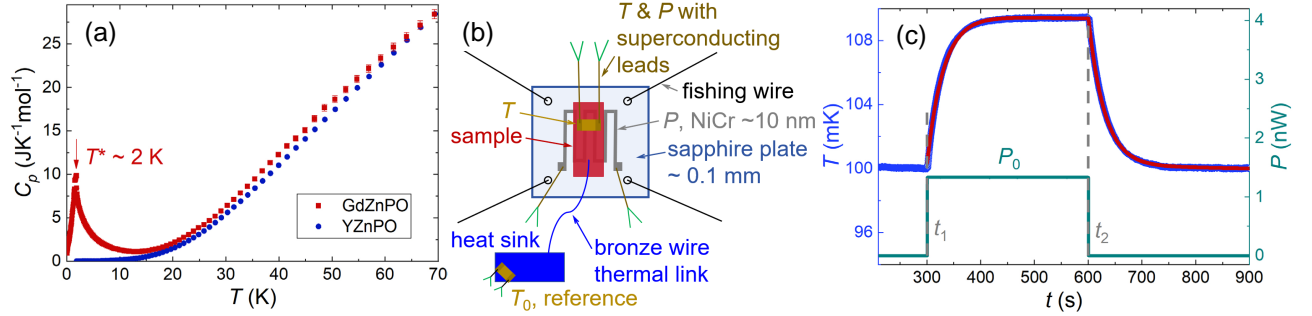


FIG. S2. (a) Specific heat of GdZnPO and YZnPO at 0 T, with the arrow representing the peak temperature  $T^* \sim 2$  K. (b) Schematic of the platform used for milli-Kelvin specific heat measurement. (c) Relaxation curve (blue) and heater power (green) for the GdZnPO single crystal at 0 T, with the red line showing a fit to the relaxation data.

an electric current to the sample heater. A  $\sim 10$  nm NiCr layer was deposited on the lower side of a 0.1 mm sapphire plate, serving as the heater. The NiCr heater’s resistance is temperature-insensitive, allowing for a perfect square wave of power ( $P$ ) by applying constant current between  $t_1$  and  $t_2$ , as shown in Fig. S2(c). Heater power was measured using 7.5-digit multimeters (DMM7510, Keithley). A plate-like single crystal of GdZnPO (mass,  $m = 0.98$  mg) was mounted on the upper side of the sapphire plate, with the magnetic field applied along the  $c$  axis ( $H^{\parallel}$ ). A thin film thermometer (CX-1010-BR, Lakeshore, marked as “ $T$ ”) mounted on the upper side of the sample was *in situ* calibrated against a reference thermometer (RX-102B-RS-0.02B, Lakeshore, calibrated down to 20 mK, marked as “ $T_0$ ”) at the start of each measurement ( $t < t_1$ ), by turning off the heater ( $P = 0$ ). The thermal link to the heat sink was provided by a thin bronze wire, adjusted to create quasi-adiabatic conditions. Each thermal relaxation measured for  $t > t_1$  can be well fitted by

$$T(t) = \Delta T[1 - \exp(-\frac{t_1 - t}{\tau})](t > t_1) - \Delta T[1 - \exp(-\frac{t_2 - t}{\tau})](t > t_2) + T_0, \quad (1)$$

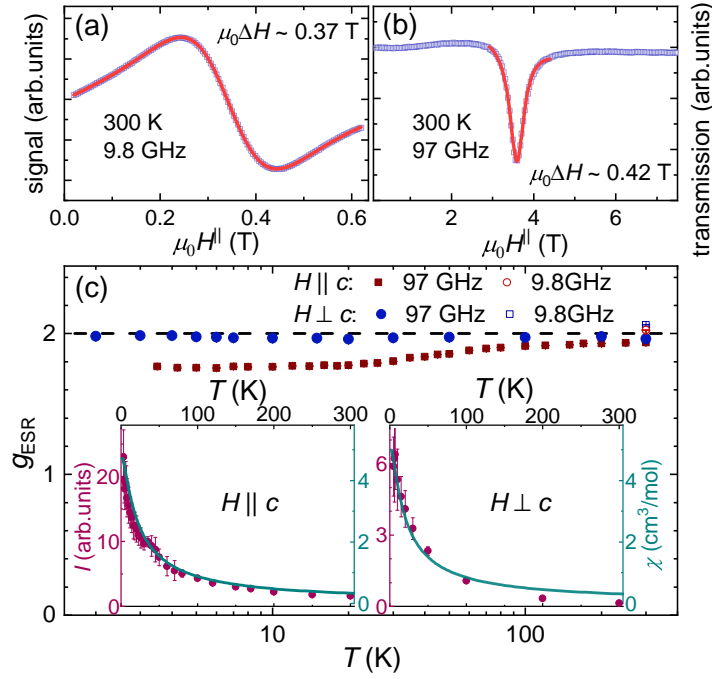


FIG. S3. (a) First-derivative ESR absorption spectrum of GdZnPO measured along the  $c$  axis at 300 K and x-band frequencies ( $\sim 9.8$  GHz). The red line shows a first-derivative Lorentzian fit. (b) Pulsed-field ESR absorption spectrum along the  $c$  axis at 300 K and 97 GHz, with the red line showing a Lorentzian fit. (c) ESR  $g$  factors. Insets compare pulsed-field ESR intensities (scatter) with bulk susceptibilities (lines) measured parallel (left) and perpendicular (right) to the  $c$  axis.

where  $\Delta T$ ,  $T_0$ , and  $\tau$  are the fitting parameters. Therefore, the molar specific heat is obtained as

$$C_p(T = T_0 + \frac{\Delta T}{2}) = \frac{M_m P_0 \tau}{m \Delta T}, \quad (2)$$

where  $M_m = 269.6$  g/mol is the molar mass. For instance, as shown in Fig. S2(c), fitting yielded  $\Delta T \sim 9.3$  mK,  $T_0 \sim 100.3$  mK, and  $\tau \sim 29.95$  s. With the measured  $P_0 = 1.333$  nW, we calculated  $C_p \sim 1.18$  JK $^{-1}$ /mol at  $T \sim 105$  mK and  $\mu_0 H^{\parallel} = 0$  T.

The first-derivative electron spin resonance (ESR) spectra were collected using a continuous-wave spectrometer (Bruker EMXmicro-6/1) at 300 K and x-band frequencies ( $\sim 9.8$  GHz) on a well-aligned single-crystal sample of GdZnPO ( $\sim 30.2$  mg), with the magnetic field applied parallel and perpendicular to the  $c$  axis [3]. Pulsed-field ESR spectra were measured during the field-increasing process at 97 GHz, down to  $\sim 2$  K, on the same sample [5–7]. Despite the frequency increase from 9.8 to 97 GHz, the ESR linewidth ( $\mu_0 \Delta H$ ) remains nearly unchanged along the  $c$  axis [compare Figs. S3(a) and S3(b)]. This is also observed in spectra measured perpendicular to the  $c$  axis,  $\mu_0 \Delta H^{\perp} = 0.36$  T at 9.8 GHz and 0.27 T at 97 GHz, at 300 K (see the main text). Therefore, we conclude that  $\mu_0 \Delta H$  remains  $\sim 0.27$ -0.42 T at  $\sim 300$  K for the GdZnPO spin system. The  $g$ -factor tensor measured at both 9.8 and 97 GHz shows good isotropy, with diagonal  $g$  factors approaching the free electron value,  $g^{\parallel} \sim g^{\perp} \sim 2$ , consistent with the zero orbit angular momentum of Gd $^{3+}$  ( $L = 0$ ). The slight decrease in  $g^{\parallel}$  as temperature cools may be attributed to the formation of easy-plane spin configurations [see Fig. S3(c)]. As shown in the insets of Fig. S3(c), ESR intensities increase with decreasing temperature, following the bulk susceptibilities. These results indicate that GdZnPO remains paramagnetic down to  $\sim 2$  K.

The aligned single-crystal sample of GdZnPO ( $\sim 30.2$  mg) was also used for magnetization ( $M$ ) measurements. Between 1.8 and 300 K, magnetization and susceptibility were measured using a magnetic property measurement system (Quantum Design) up to 7 T. At 1.9 and 4.2 K, magnetization was measured up to 14 T with a vibrating sample magnetometer in a PPMS. For measurements between 0.03 and 1.9 K, a high-resolution Faraday force magnetometer in the  $^3\text{He}$ - $^4\text{He}$  dilution refrigerator was used, with 13 mg of aligned crystals. Main magnetic fields ( $\mu_0 |H^{\parallel}| \leq 12$  T) and field gradients ( $\mu_0 |dH^{\parallel}/dz| \leq 10$  T/m) were generated by superconducting coils (in INTA-LLD-S12/14, Oxford Instruments). The electric capacitance ( $c_e$ ) was measured using a  $f = 1$  kHz ultra-precision capacitance bridge (AH-2500A, Andeen-Hagerling) with the three-terminal method [8–10]. The parallel loss  $l_p \sim -0.036$  nS was negligible, and the parallel capacitance  $c_p \sim 3.4$  pF or series capacitance  $c_s$  was nearly equal to  $c_e$ , with  $c_s/c_p - 1 = l_p^2/(2\pi f c_p)^2 \sim 2.8 \times 10^{-6}$ , comparable to the noise-to-signal ratio of  $c_p$  ( $\sim 1.5 \times 10^{-6}$ ). Thus,  $c_p$  was used directly as the capacitance of the magnetometer,  $c_e$ , for simplicity. The change in inverse capacitance between two

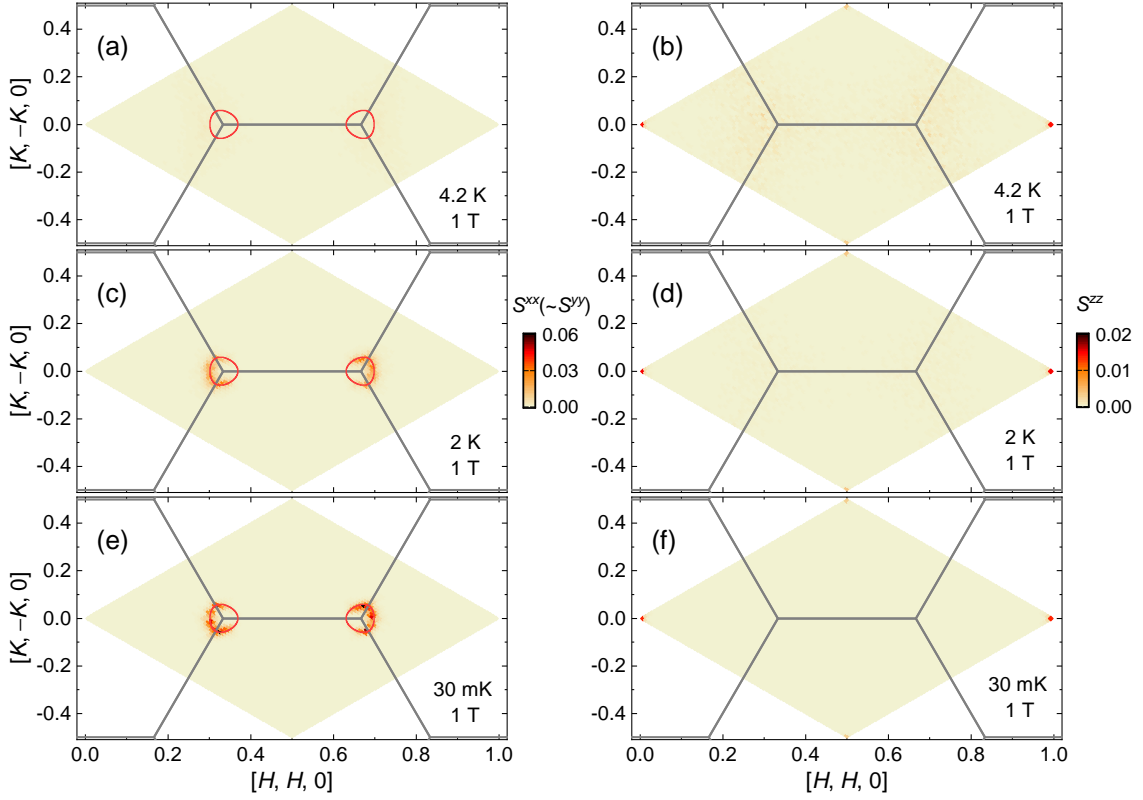


FIG. S4. Spin structure factors  $S^{xx}$  ( $\sim S^{yy}$ ) [(a), (c), (e)] and  $S^{zz}$  [(b), (d), (f)] calculated at  $\mu_0 H^{\parallel} = 1$  T. Red lines represent the spiral contour [Eq. (8)], and grey lines denote Brillouin zone boundaries. Panels (a), (c), and (e) for  $S^{xx}$  share the same scale, as do panels (b), (d), and (f) for  $S^{zz}$ .

different gradients (e.g.,  $-10$  and  $10$  T/m) is given by

$$\Delta\left(\frac{1}{c_e}\right) = M^{\parallel} \frac{\mu_0 \mu_B N}{k_{\text{eff}} \epsilon_0 A} \Delta\left(\frac{dH^{\parallel}}{dz}\right) \propto M^{\parallel}, \quad (3)$$

where  $\epsilon_0$  is the vacuum permittivity,  $A$  is the area of the polar plate,  $k_{\text{eff}}$  is the effective spring coefficient in Hooke's law, and  $N$  is the number of  $\text{Gd}^{3+}$  spins. Scaling to  $M^{\parallel}$  measured by PPMS,  $k_{\text{eff}} \sim 1.7$  kN/m was obtained below  $\sim 1.9$  K for the magnetometer.

## II. SPIRAL SPIN-LIQUID ANSATZ

The combined Monte Carlo (MC) fit suggests that the spin Hamiltonian of  $\text{GdZnPO}$  can be approximated as

$$\mathcal{H} = J_1 \sum_{\langle j_0, j_1 \rangle} \mathbf{S}_{j_0} \cdot \mathbf{S}_{j_1} + J_2 \sum_{\langle\langle j_0, j_2 \rangle\rangle} \mathbf{S}_{j_0} \cdot \mathbf{S}_{j_2} + D \sum_{j_0} (S_{j_0}^z)^2 - \mu_0 H^{\parallel} g \mu_B \sum_{j_0} S_{j_0}^z, \quad (4)$$

where  $J_1 \sim -0.39$  K and  $J_2 \sim 0.57$  K are the first- ( $\langle \rangle$ ) and second- ( $\langle\langle \rangle\rangle$ ) nearest-neighbor couplings, respectively, and  $D \sim 0.30$  K represents an easy-plane anisotropy. These interactions lead to spin frustration on the honeycomb lattice. The ground-state phase is expected to be a spiral spin liquid (SSL), with spin vectors on the  $A$  and  $B$  sublattices given by [11]

$$\mathbf{S}_A = S[\cos \psi \cos(\mathbf{Q} \cdot \mathbf{R}), \cos \psi \sin(\mathbf{Q} \cdot \mathbf{R}), \sin \psi] \quad \text{and} \quad (5)$$

$$\mathbf{S}_B = S[\cos \psi \cos(\mathbf{Q} \cdot \mathbf{R} + \phi), \cos \psi \sin(\mathbf{Q} \cdot \mathbf{R} + \phi), \sin \psi], \quad (6)$$



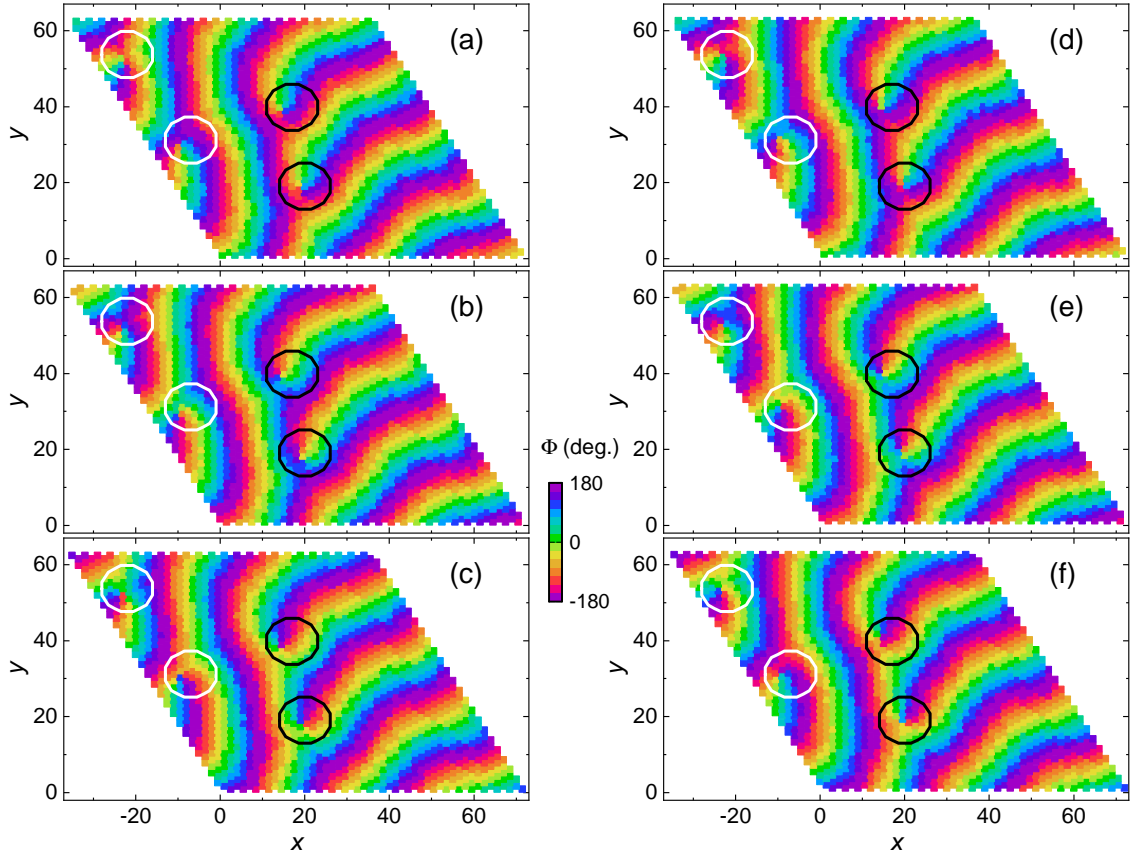


FIG. S5. Spin configuration projected onto the  $ab$  plane,  $\Phi = -i \ln \frac{S^x + iS^y}{\sqrt{(S^x)^2 + (S^y)^2}}$ , calculated at 30 mK and  $\mu_0 H^\parallel = 1$  T for sublattices  $A$  I (a),  $A$  II (b),  $A$  III (c),  $B$  I (d),  $B$  II (e), and  $B$  III (f). White and black circles indicate spin vortices and antivortices, respectively. All panels share the same  $\Phi(\mathbf{r})$  scale, with highlighted vortex and antivortex loops unchanged across panels.

where  $\mathbf{R}$  is the unit cell position,  $\mathbf{Q} = h\mathbf{b}_1 + k\mathbf{b}_2$  is the ordering wave vector, and  $\mathbf{b}_1, \mathbf{b}_2$  are reciprocal lattice vectors. The energy per site is given by

$$E = \left(D + \frac{3J_1}{2} + 3J_2\right)S^2 \sin^2 \psi + h_Z S \sin \psi + \frac{J_1 S^2 \cos^2 \psi}{2} [\cos \phi + \cos(\phi - 2\pi h) + \cos(\phi - 2\pi h - 2\pi k)] + J_2 S^2 \cos^2 \psi [\cos(2\pi h) + \cos(2\pi k) + \cos(2\pi h + 2\pi k)], \quad (7)$$

where  $h_Z = -\mu_0 H^\parallel g \mu_B$ . Minimizing this expression, we find  $\cos \phi = \frac{f_1}{\sqrt{f_1^2 + f_2^2}}$ ,  $\sin \phi = \frac{f_2}{\sqrt{f_1^2 + f_2^2}}$ , and  $\sin \psi = -\frac{h_Z}{2S\eta}$ , where  $f_1 = 1 + \cos(2\pi h_G) + \cos(2\pi h_G + 2\pi k_G)$ ,  $f_2 = \sin(2\pi h_G) + \sin(2\pi h_G + 2\pi k_G)$ , and  $\eta = D + \frac{3J_1}{2} + \frac{9J_2}{2} + \frac{J_1^2}{8J_2}$ . The spiral contour is given by

$$\cos(2\pi h_G) + \cos(2\pi k_G) + \cos(2\pi h_G + 2\pi k_G) = \frac{1}{2} \left( \frac{J_1^2}{4J_2^2} - 3 \right). \quad (8)$$

Finally, the zero-temperature energy and magnetization are analytically expressed as

$$E_0 = -\frac{h_Z^2}{4\eta} - \left( \frac{J_1^2}{8J_2} + \frac{3J_2}{2} \right) S^2 \text{ for } |h_Z| \leq 2S\eta, \quad E_0 = \left( D + \frac{3J_1}{2} + 3J_2 \right) S^2 + h_Z S \text{ for } |h_Z| > 2S\eta, \quad (9)$$

$$M^\parallel = -\frac{h_Z g}{2\eta} \text{ for } |h_Z| \leq 2S\eta, \text{ and } |M^\parallel| = Sg \text{ for } |h_Z| > 2S\eta. \quad (10)$$

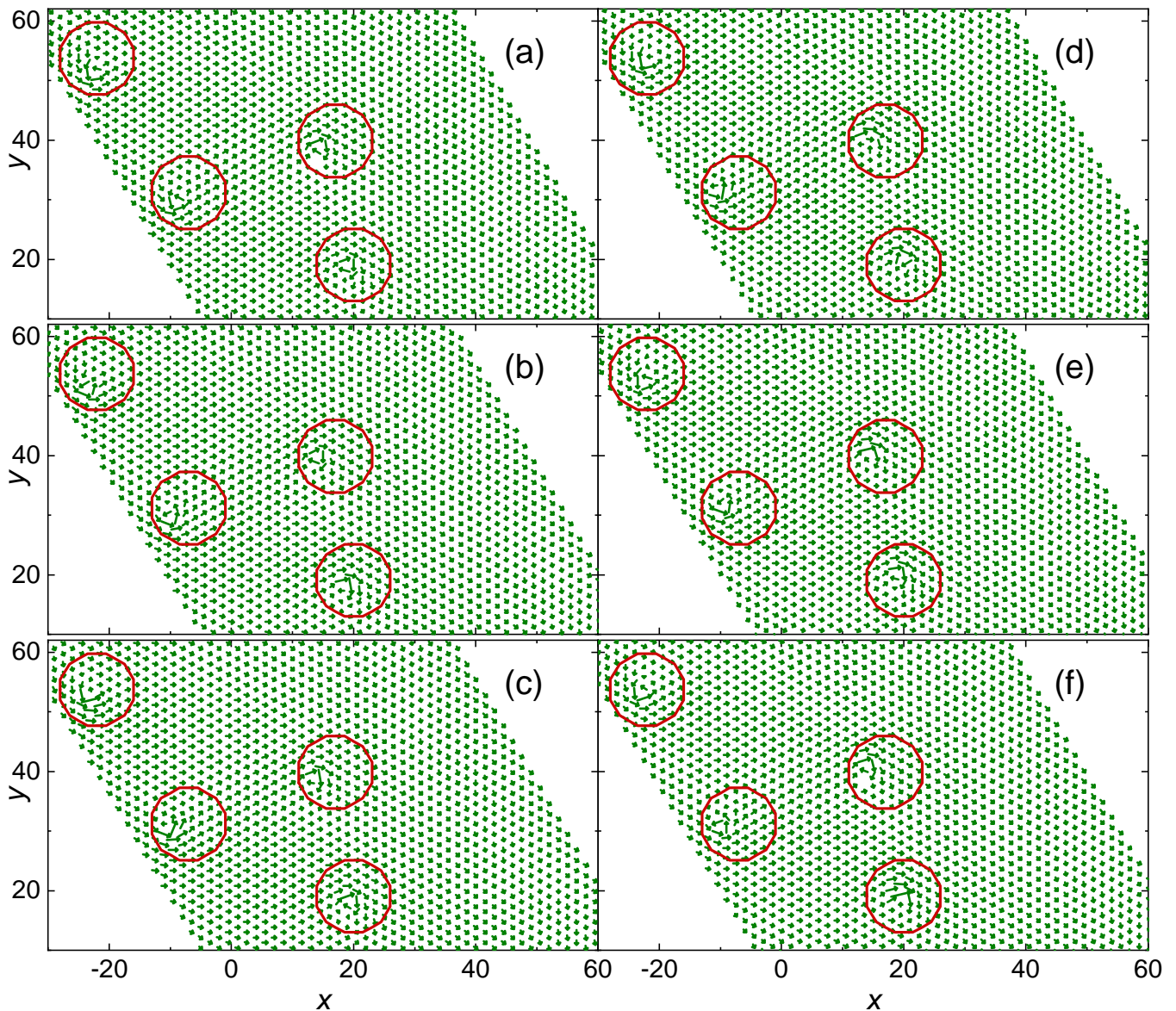


FIG. S6. Sublattice gradient of the spin configuration,  $\nabla\Phi(\mathbf{r})$ , on sublattices *A I* (a), *A II* (b), *A III* (c), *B I* (d), *B II* (e), and *B III* (f). Local momentum vortices (red circles) appear around the same positions as the topological defects shown in Fig. S5.

### III. MONTE CARLO SIMULATIONS AND LOW-ENERGY TOPOLOGICAL DEFECTS.

We conducted unbiased MC simulations on  $2 \times L_N^2$  clusters with periodic boundary conditions using the determined spin Hamiltonian of GdZnPO. In Fig. 2 of the main text, we employed an  $L_N = 9$  cluster, averaged over 40 independent samples, to fit the magnetization data above 1.9 K. For Fig. 4 in the main text, we used an  $L_N = 72$  cluster in panel (a), an  $L_N = 15$  cluster averaged over 64 independent samples in panel (b) [also in Fig. 3(b) of the main text], an  $L_N = 72$  cluster averaged over 20 independent samples in panels (c) and (d) (also in Fig. S4), and an  $L_N = 72$  cluster in panels (e) and (f) (also in Figs. S5-S7). Figs. S5-S7 depict the same spin state. A total of 5,000 to 10,000 MC steps were performed, with 500 to 4,000 steps allocated for thermalization. The energy became nearly independent of the number of MC steps after approximately 200 steps, at  $T \geq 0.03$  K.

At 30 mK, the MC energy per spin  $E$  agrees well with the analytical energy  $E_0$  calculated using Eq. (9) [see Fig. 4(a) in the main text]. More specifically,  $E_0$  is consistently lower than  $E$  across various magnetic fields, with  $E - E_0 \sim 0.1$  K/spin, supporting the validity of the ground-state ansatz given by Eqs. (5) and (6). Additionally, the low-temperature MC magnetization

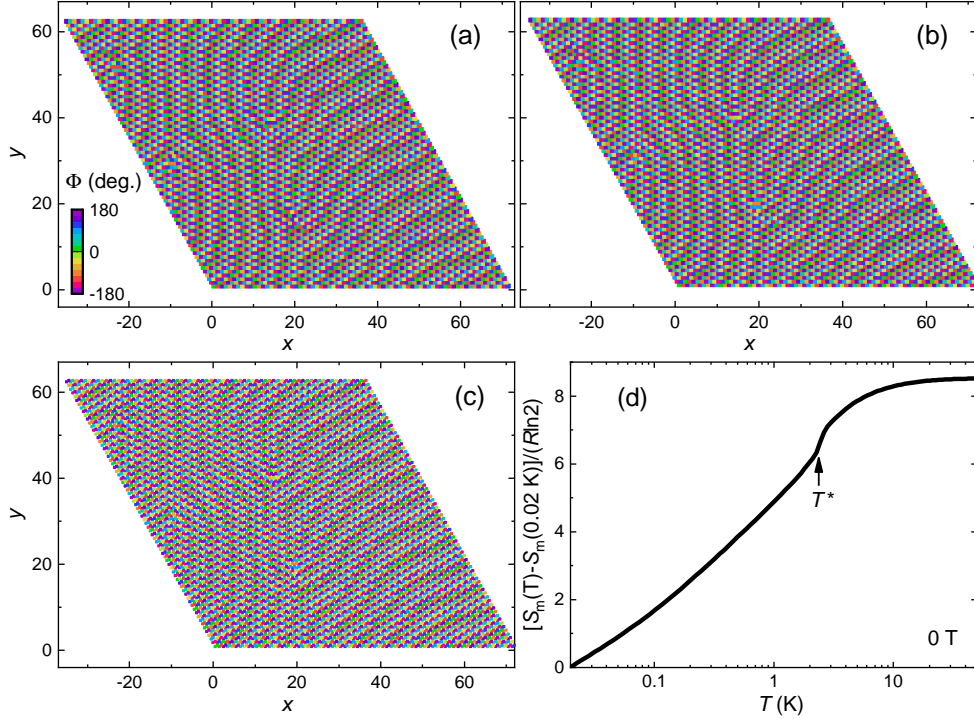


FIG. S7. The spin configuration projected onto the  $ab$  plane,  $\Phi = -i \ln \frac{S^x + iS^y}{\sqrt{(S^x)^2 + (S^y)^2}}$ , calculated at 30 mK and  $\mu_0 H^\parallel = 1$  T for sublattice  $A$  (a), sublattice  $B$  (b), and the entire honeycomb lattice (c). Panels (a)-(c) share the same  $\Phi(\mathbf{r})$  scale, as shown in panel (a). (d) Entropy increase  $S_m(T) - S_m(0.02 \text{ K})$  at 0 T, calculated using classical Monte Carlo simulations, with the crossover temperature  $T^*$  indicated.

aligns well with the zero-temperature magnetization predicted by Eq. (10).

The MC specific heat ( $C_m$ ) shows a peak at  $T^* \sim 2$  K [see Fig. 4(b) in the main text], which is roughly consistent with the experimental data [see Fig. S2(a)]. To understand the entropy release around  $T^*$ , we analyzed the spin configurations at various temperatures. At high temperatures (e.g., 50 K,  $\gg |J_1|S^2$ ), the spins exhibit no orientation preference, and  $C_m$  remains low, as the average absolute components approach their high- $T$  limits,  $\langle |S^\perp| \rangle = \langle \sqrt{(S^x)^2 + (S^y)^2} \rangle \rightarrow \frac{S}{2} \int_0^\pi \sin^2 \theta d\theta (= \frac{\pi S}{4})$  and  $\langle |S^z| \rangle \rightarrow \frac{S}{2} \int_0^\pi \sin \theta |\cos \theta| d\theta (= \frac{S}{2})$ . As the temperature decreases,  $\langle |S^\perp| \rangle$  approaches 1 and  $\langle |S^z| \rangle$  approaches 0 near the specific heat peak, signaling the formation of coplanar spin configurations in the  $ab$  plane due to easy-plane anisotropy  $D$ . This entropy release is primarily attributed to the transition from a three-dimensional spin configuration at higher temperatures to a two-dimensional one as the system cools. Additionally, the transition from a thermally paramagnetic phase to the low-temperature SSL, which spontaneously breaks chiral symmetry at  $T^*$  [12], also contributes to the specific heat peak.

We further computed the spin structure factors (Fig. S4),

$$S^{\alpha\alpha}(\mathbf{k}) = \langle |\frac{1}{N} \sum_j S_j^\alpha \exp(i\mathbf{k} \cdot \mathbf{R}_j)|^2 \rangle, \quad \alpha = x, y, \text{ or } z, \quad (11)$$

where  $\mathbf{R}_j$  represents the position of the  $j$ th spin on the honeycomb lattice,  $N = 2 \times 72^2 = 10,368$  is the total number of spins, and  $\langle \rangle$  denotes an average over 20 independent samples. Below  $T^*$ ,  $S^{xx}$  ( $\sim S^{yy}$ ) exhibits significant intensity around the spiral contour [Eq. (8)], with this intensity increasing as the temperature decreases [compare Figs. S4(e) and S4(c)]. In contrast,  $S^{zz}$  shows an intensity of  $\sim S^2 \sin^2 \psi$  at the  $\Gamma$  point, which remains almost constant below  $\sim 4.2$  K [see Figs. S4(b), S4(d), and S4(f)], consistent with the SSL ansatz. For magnetic fields  $-h_z$  between 0 and the saturation value  $-h_z^s = 2S\eta$ , the in-plane spin components exhibit incommensurate order, while the out-of-plane components form ferromagnetic order, below  $T^*$ . Therefore,  $T^*$  is also related to the transition between the SSL and thermally paramagnetic phases. Moreover, no clear evidence of “order by disorder” [13, 14] was observed in the MC simulations, down to the lowest experimentally achievable temperature of  $\sim 30$  mK, in agreement with experimental observations (see the main text).

- 
- [1] H. Lincke, R. Glaum, V. Dittrich, M. Tegel, D. Johrendt, W. Hermes, M. H. Möller, T. Nilges, and R. Pöttgen, “Magnetic, optical, and electronic properties of the phosphide oxides REZnPO (RE = Y, La-Nd, Sm, Gd, Dy, Ho),” *Z. Anorg. Allg. Chem.* **634**, 1339 (2008).
- [2] Y. Li, S. Bachus, H. Deng, W. Schmidt, H. Thoma, V. Hutanu, Y. Tokiwa, A. A. Tsirlin, and P. Gegenwart, “Partial up-up-down order with the continuously distributed order parameter in the triangular antiferromagnet TmMgGaO<sub>4</sub>,” *Phys. Rev. X* **10**, 011007 (2020).
- [3] B. Li, X. Chen, Y. Zhao, Z. Ma, Z. Wan, and Y. Li, “Proximate Tomonaga-Luttinger liquid in a spin-1/2 ferromagnetic XXZ chain compound,” *Phys. Rev. Mater.* **8**, 074410 (2024).
- [4] B. Li, Z. Wan, Y. Song, Z. Ma, Y. Zhao, J. Wang, and Y. Li, “Frustrated magnetism of the spin-1 kagome antiferromagnet  $\beta$ -BaNi<sub>3</sub>(VO<sub>4</sub>)<sub>2</sub>(OH)<sub>2</sub>,” *J. Phys.: Condens. Matter* **35**, 505801 (2023).
- [5] X. Y. Yue, Z. W. Ouyang, J. F. Wang, Z. X. Wang, Z. C. Xia, and Z. Z. He, “Magnetization and ESR studies on Cu<sub>4</sub>(OH)<sub>6</sub>FCI: An antiferromagnet with a kagome lattice,” *Phys. Rev. B* **97**, 054417 (2018).
- [6] X. P. Jin, Z. W. Ouyang, X. C. Liu, T. T. Xiao, J. J. Cao, Z. X. Wang, Z. C. Xia, and W. Tong, “Two-sublattice description of the dimer-trimer chain compound Li<sub>2</sub>Cu<sub>5</sub>Si<sub>4</sub>O<sub>14</sub>: High-field magnetization and ESR studies,” *Phys. Rev. B* **104**, 174423 (2021).
- [7] Z. Zhang, Y. Cai, J. Kang, Z. Ouyang, Z. Zhang, A. Zhang, J. Ji, F. Jin, and Q. Zhang, “Anisotropic exchange coupling and ground state phase diagram of Kitaev compound YbOCl,” *Phys. Rev. Res.* **4**, 033006 (2022).
- [8] Y. Shimizu, Y. Kono, T. Sugiyama, S. Kittaka, Y. Shimura, A. Miyake, D. Aoki, and T. Sakakibara, “Development of high-resolution capacitive Faraday magnetometers for sub-Kelvin region,” *Rev. Sci. Instrum.* **92**, 123908 (2021).
- [9] Y. Zhao, Z. Ma, Z. He, H. Liao, Y.-C. Wang, J. Wang, and Y. Li, “Quantum annealing of a frustrated magnet,” *Nat. Commun.* **15**, 3495 (2024).
- [10] Y. Li, S. Bachus, B. Liu, I. Radelytskyi, A. Bertin, A. Schneidewind, Y. Tokiwa, A. A. Tsirlin, and P. Gegenwart, “Rearrangement of uncorrelated valence bonds evidenced by low-energy spin excitations in YbMgGaO<sub>4</sub>,” *Phys. Rev. Lett.* **122**, 137201 (2019).
- [11] K. Fujiwara, S. Kitamura, and T. Morimoto, “Thermal Hall responses in frustrated honeycomb spin systems,” *Phys. Rev. B* **106**, 035113 (2022).
- [12] C.-J. Huang, J. Q. Liu, and G. Chen, “Spiral spin liquid behavior and persistent reciprocal kagome structure in frustrated van der Waals magnets and beyond,” *Phys. Rev. Res.* **4**, 013121 (2022).
- [13] S. Okumura, H. Kawamura, T. Okubo, and Y. Motome, “Novel spin-liquid states in the frustrated Heisenberg antiferromagnet on the honeycomb lattice,” *J. Phys. Soc. Jpn.* **79**, 114705 (2010).
- [14] T. Shimokawa, T. Okubo, and H. Kawamura, “Multiple- $q$  states of the  $J_1$ - $J_2$  classical honeycomb-lattice Heisenberg antiferromagnet under a magnetic field,” *Phys. Rev. B* **100**, 224404 (2019).